*J. Fluid Mech.* (2002), *vol.* 463, *pp.* 229–239.  
DOI: 10.1017/S0022112002008807 Printed in the United Kingdom

# Linear three-dimensional instability of a magnetically driven rotating flow

By I. GRANTS AND G. GERBETH†

Forschungszentrum Rossendorf, Postfach 510119, 01314 Dresden, Germany

(Received 22 November 2001 and in revised form 4 February 2002)

The instability of a rotating-magnetic-field-driven liquid metal flow in a finite cylinder with respect to infinitesimal azimuthally periodic perturbations is studied numerically. This instability is observed to set in prior its axisymmetric counterpart with relatively low frequency at diameter-to-height ratios between 0.5 and 2. The axisymmetric and three-dimensional instabilities have similar characteristic features. The instability originates in the cross-section of the horizontal and vertical rotating boundary layers and excites inertial waves in the inviscid core.

## 1. Introduction

A rotating magnetic field (RMF) induces an azimuthal body force in a column of liquid metal. The resulting flow in a finite cylinder consists of an inviscid almost rigidly rotating core separated from the rigid walls by pronounced boundary layers (e.g. Grants & Gerbeth 2001 and references therein). Thus, one expects the Taylor–Görtler instability of the side layer (see the review by Saric 1994) and the instability of the Bödewadt-type horizontal layer (Savaş 1987; Lopez & Weidman 1996; Lingwood 1997) to occur at a certain order depending on the aspect ratio. The subject is complicated by the fact that the Taylor–Görtler rolls are triggered by a small finite perturbation via a non-normal–nonlinear transition mechanism in the linearly stable regime. Such a transition may occur over a broad control parameter range depending on the shape and amplitude of finite disturbances, as is often observed in various shear flows (see the review by Grossmann 2000). As is typical for such cases, the basic flow is marked by degenerated leading eigenmodes. Thus, the small perturbations, being poorly spanned by the eigendirections, may grow considerably in energy. This is known as energetical instability. This linear phenomenon may amplify the energy of the initial perturbation by orders of magnitude. However, after reaching the maximum such a perturbation decays rapidly if it is not attracted by a system of saddle-type fixed points, representing another pivotal feature of a dynamical system under non-normal–nonlinear transition. Once the phase trajectory enters the domain of attraction of these additional solutions it moves between them for much longer times than prescribed by the decaying eigenmodes of the basic solution. We have found (Grants & Gerbeth 2001) that the minimum amplitude of an unstable perturbation decreases with the relative diameter of the cylinder and becomes smaller than $10^{-6}$ for a diameter-to-height ratio 0.25. Thus, the axisymmetric flow may behave chaotically though the basic state is still linearly stable to axisymmetric perturbations.

The three-dimensional instability of the RMF-driven flow has not been considered

† Author to whom correspondence should be addressed: gerbeth@fz-rossendorf.de

up to now, partially due to a lack of understanding of the axisymmetric flow dynamics. Tomasino & Marty (2000) reported an almost negligible departure from the axial symmetry in their numerical three-dimensional simulations of the RMF-driven flow. However, no systematic stability analysis was performed. Volz & Mazuruk (2001) experimentally investigated the influence of an RMF on Rayleigh–Bénard convection in a cylindrical column of liquid gallium with an aspect ratio of 1. They found an onset of oscillations independent of the temperature field at an RMF driving force some 10% below the two-dimensional instability limit. There is experimental (Escudier 1984) and numerical evidence (Gelfgat, Bar-Yoseph & Solan 2001) that the related lid-driven flow instability is axisymmetric in a certain range of aspect ratios around unity. The numerical analysis revealed that the instability is three-dimensional both in a more elongated and a flattened cylinder.

Initially, our objective was to identify the aspect ratio range in which the axisymmetric linear instability prevails in the RMF-driven flow. We addressed the problem by employing a numerical time integration of the linearized Navier–Stokes equation for separate azimuthal modes. After some transient filtering time the solution contained only a few leading eigenmodes that were separated by a simple and efficient method (Goldhirsch, Orszag & Maulik 1987). We found that the linear three-dimensional instability is similar in appearance but sets in well before its axisymmetric counterpart for the aspect ratios considered. We also found that the instability originates in the corner. Thus, the boundary layer instability results do not apply despite these layers being thin and pronounced.

## 2. Formulation of the problem

We consider a small three-dimensional perturbation $\boldsymbol{v}$ superimposed on the axisymmetric basic flow $\boldsymbol{U}$ of an incompressible Newtonian fluid with kinematic viscosity $\nu$, in a cylinder of radius $R_0$ and height $2H_0$. Neglecting the higher-order small nonlinearity the dynamics of such a perturbation is described by

$$\frac{\partial \boldsymbol{v}}{\partial t} + \boldsymbol{\omega} \times \boldsymbol{U} + \boldsymbol{\Omega} \times \boldsymbol{v} = \nabla^2 \boldsymbol{v} - \nabla P \tag{2.1}$$

$$\nabla \cdot \boldsymbol{v} = 0, \tag{2.2}$$

where $\boldsymbol{\Omega} = \nabla \times \boldsymbol{U}$ and $\boldsymbol{\omega} = \nabla \times \boldsymbol{v}$. The no-slip boundary conditions are

$$\boldsymbol{v}|_{\mathscr{D}} = 0, \tag{2.3}$$

where $\mathscr{D}$ stands for the surface of the domain. The scales $\nu/H_0$, $H_0^2/\nu$ and $H_0$ or $R_0$ were used in equations (2.1) and (2.2) for velocity, time and axial or radial coordinate, respectively. The basic flow $\boldsymbol{U}$ is driven by a low-frequency low-induction rotating magnetic field forcing an azimuthal rotation of the liquid. The so-called Ekman pumping generates radial inflow jets near the stationary horizontal walls. Two toroidal vortices result, providing a radial outward flow in the bulk of the column. For more details of the basic flow and its axisymmetric stability we refer to Grants & Gerbeth (2001). The problem is determined by two governing parameters: the aspect ratio $R = R_0/H_0$ and the magnetic Taylor number $Ta = \omega\sigma B_0^2 H_0^4/(2\nu^2\rho)$ where $\omega$ and $B_0$ are angular frequency and induction of the RMF, and $\sigma$ and $\rho$ are electric conductivity and density of the liquid, respectively.

## 3. Numerical techniques

### 3.1. *Spectral presentation*

An arbitrary perturbation $\boldsymbol{v}(r,\phi,z,t)$ can be decomposed into azimuthal modes $\boldsymbol{v}^m(r,z,t)\,\mathrm{e}^{\mathrm{i}m\phi}$ that are independent in the linear approximation. The basic flow under consideration has certain vertical symmetries $U_r(r,z) = U_r(r,-z)$, $U_\phi(r,z) = U_\phi(r,-z)$ and $U_z(r,z) = -U_z(r,-z)$. Taking into account this vertical symmetry of $\boldsymbol{U}$ the Chebyshev expansion of the perturbation can be split into independent symmetric

$$v_r^{m+}(r,z,t) = \sum_{i=1}^{N}\sum_{j=1}^{M-1+p} v_{ij}^{m+}(t)T_{2i-2}(z)T_{2j-1-p}(r), \tag{3.1}$$

$$v_\phi^{m+}(r,z,t) = \sum_{i=1}^{N}\sum_{j=1}^{M-1+p} u_{ij}^{m+}(t)T_{2i-2}(z)T_{2j-1-p}(r), \tag{3.2}$$

$$v_z^{m+}(r,z,t) = \sum_{i=1}^{N-1}\sum_{j=1}^{M-p} w_{ij}^{m+}(t)T_{2i-1}(z)T_{2j-2+p}(r) \tag{3.3}$$

and antisymmetric

$$v_r^{m-}(r,z,t) = \sum_{i=1}^{N-1}\sum_{j=1}^{M-1+p} v_{ij}^{m-}(t)T_{2i-1}(z)T_{2j-1-p}(r), \tag{3.4}$$

$$v_\phi^{m-}(r,z,t) = \sum_{i=1}^{N-1}\sum_{j=1}^{M-1+p} u_{ij}^{m-}(t)T_{2i-1}(z)T_{2j-1-p}(r), \tag{3.5}$$

$$v_z^{m-}(r,z,t) = \sum_{i=1}^{N}\sum_{j=1}^{M-p} w_{ij}^{m-}(t)T_{2i-2}(z)T_{2j-2+p}(r) \tag{3.6}$$

parts, where $T_n(x) = \cos(n\arccos(x))$ are the orthogonal Chebyshev polynomials and $p$ is the remainder of $m/2$, i.e. $p = 0$ for even $m$ or $p = 1$ for odd $m$. Since the velocity is a real-valued function, only positive wavenumbers are considered. The radial dependence of the components (3.1)–(3.6) includes only radial coordinate modes of appropriate parity: the parity of the $v_z$ radial dependence is equal to the parity of the wavenumber $m$. Thus, the radial coordinate expansions (3.3) and (3.6) contain only even terms for even $m$ and only odd terms for odd $m$. The parity of $v_r$ and $v_\phi$ is opposite to that of $v_z$. It can be easily verified (e.g. Grants & Gerbeth 2001) that this is necessary (not sufficient) for the expressions (3.1)–(3.6) to be infinitely differentiable for $r \leqslant 1$. The corresponding nodal presentation is defined on the Gauss–Lobatto mesh in a square $[0:1]\times[0:1]$.

### 3.2. *Temporal approximation*

The third-order temporal approximation of (2.1) at time step $t^{n+1}$ is written

$$\frac{11}{6\Delta t}\boldsymbol{v}^{n+1} - \frac{1}{3\Delta t}\left(\boldsymbol{v}^n - \frac{\boldsymbol{v}^{n-1}}{2} + \frac{\boldsymbol{v}^{n-2}}{9}\right) = \nabla^2\boldsymbol{v}^{n+1} + 3\boldsymbol{q}^n - 3\boldsymbol{q}^{n-1} + \boldsymbol{q}^{n-2} - \nabla P, \tag{3.7}$$

where $\boldsymbol{q} = -(\boldsymbol{\omega}\times\boldsymbol{U} + \boldsymbol{\Omega}\times\boldsymbol{v})$. The scheme is fully implicit for the diffusive term while the convective term is explicitly extrapolated from three previous time steps. This leads to the Helmholtz equation for a divergence-free vector field, where the incompressibility is adjusted by $P$.

### 3.3. *Pressure boundary conditions*

By taking the divergence of equation (3.7) we obtain a Poisson equation for the pressure $P$ in the form

$$\nabla^2 P = \nabla \cdot \boldsymbol{Q}. \tag{3.8}$$

The boundary conditions are evaluated by means of the spectral dependence matrix (Tuckerman 1989; Canuto *et al.* 1988). Initially the zero-pressure boundary conditions are applied at each time step, and the corresponding $\nabla \cdot \boldsymbol{v}|_{\mathscr{D}}$ is evaluated. The spectral dependence matrix 'translates' this into the Dirichlet boundary condition for pressure $P|_{\mathscr{D}} = P_{BC}$ with which $\nabla \cdot \boldsymbol{v}|_{\mathscr{D}} = 0$. The spectral dependence matrix is evaluated once at the beginning of the simulation for a given time step $\Delta t$.

### 3.4. *Solution of the Helmholtz equation*

The Helmholtz vector equation (3.7) couples the $v_\phi$ and $v_r$ components, but the variables $s_+ = v_\phi + \mathrm{i}v_r$ and $s_- = v_\phi - \mathrm{i}v_r$ decouple (Tuckerman 1989). The resulting scalar Helmholtz equations were solved with the collocation approximation for the radial part of the Laplace operator, yielding a real spectrum. The usual Chebyshev tau approximation was applied in the axial direction. Such a combination of different approximations enabled a conventional diagonalization of the radial operator in combination with a fast factorization of the axial dependence in $O(NM)$ operations (Canuto *et al.* 1988).

### 3.5. *Evaluation of the leading eigenvalue and eigenvector*

After discretization the equations (2.1) and (2.2) in terms of the unknown time-dependent coefficients in equations (3.1)–(3.3) or (3.4)–(3.6) may be put into the canonical form $\dot{\boldsymbol{x}} = \boldsymbol{A}\boldsymbol{x}$ where $\boldsymbol{A}$ is a general complex non-symmetric matrix. The flow is linearly unstable if there is an eigenvalue of $\boldsymbol{A}$ with a positive real part. Thus, to solve the instability problem the matrix $\boldsymbol{A}$ and its full spectrum must be evaluated. There is an alternative way of finding the leading eigenvectors and eigenvalues (those with the maximum real part) as introduced by Goldhirsch *et al.* (1987). Given the solution vector $\boldsymbol{x}$ as a linear combination of a few leading eigenmodes at a few equidistant time intervals ($t = (l-1)\tau$, $l = 1, 2, \ldots, L$) this method evaluates these modes and corresponding eigenvalues. In that way, the stability problem reduces to the time integration of (3.7). We perturbed the flow with a divergence-free perturbation satisfying the appropriate boundary and pole conditions:

$$v_r^+(r,\phi,z) = (P_1(z)Q_1(r) + \mathrm{i}P_2(z)Q_2(r))r^{m-1}\,\mathrm{e}^{\mathrm{i}m\phi}, \tag{3.9}$$

$$v_z^+(r,\phi,z) = z(Q_1(z)P_1(r) + \mathrm{i}Q_2(z)P_2(r))r^{m-1}\,\mathrm{e}^{\mathrm{i}m\phi}, \tag{3.10}$$

$$v_\phi^+(r,\phi,z) = \frac{\mathrm{i}}{m}\left(r\frac{\partial v_r^+}{\partial r} + v_r^+ + Rr\frac{\partial v_z^+}{\partial z}\right), \tag{3.11}$$

or

$$v_r^-(r,\phi,z) = zv_r^+, \quad v_z^- = \frac{v_z^+}{z}, \quad v_\phi^- = \frac{\mathrm{i}}{m}\left(r\frac{\partial v_r^-}{\partial r} + v_r^- + Rr\frac{\partial v_z^-}{\partial z}\right), \tag{3.12}$$

with $P_i = 1-x^{2i}$, $Q_i = 1-((i+1)x^2-x^{2+2i})/i$ and integrated (3.7) over a certain filtering time $\tau_{filt} \approx 2\Omega_0^{-1/2}/m$, where $\Omega_0$ is the characteristic rotation rate of the basic flow. After this time the solution contained (within 0.01% tolerance) only a few (some 5 to 30) eigenmodes that were separated by the method of Goldhirsch *et al.* (1987). This approach saves a considerable amount of computational time and computer memory

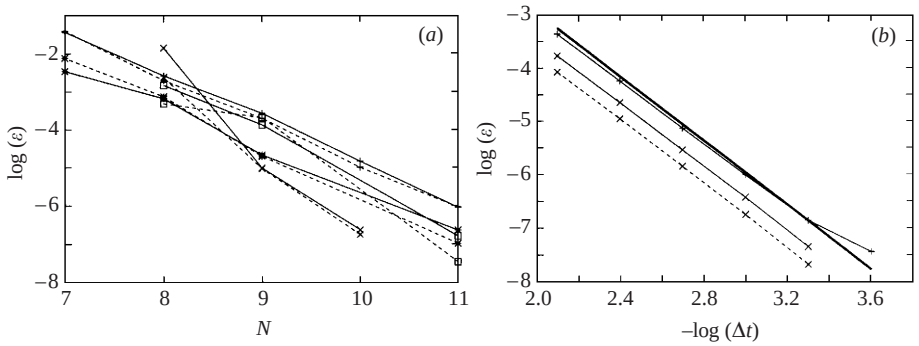


FIGURE 1. The maximum absolute error of the numerical test solution versus: (*a*) spatial resolution; (*b*) time step. The solid and dashed lines mark symmetric and antisymmetric solutions, respectively. The symbols $+ \times \boxdot *$ correspond to wavenumbers $m = 1$–4, respectively. The thick line displays the $(\Delta t)^{-3}$ slope.

for large eigenvalue problems since the full matrix need not be evaluated, stored and decomposed. The method should be used with caution, however, since spurious eigenvalues may be obtained. For instance, the numerical approximation error may be misinterpreted as an eigenmode. These artifacts have small characteristic amplitude. To eliminate them, the equations were additionally (where needed) integrated in time until the amplitude of the leading eigenmode found was at least 30% of the largest amplitude. To check the leading eigenmode obtained we took it as the initial state integrated over time $\tau_{filt}$ and approximated the time history of $u_{11}(t)$ with a function $A\,\mathrm{e}^{\lambda t}$ by means of a nonlinear least-squares Marquardt–Levenberg algorithm. The eigenvalue search procedure was repeated with a different filtering time $\tau_{filt}$ and/or the sampling interval $\tau$ if the absolute value of the leading eigenvalue $\lambda = \lambda_r + \mathrm{i}\lambda_i$ differed by more than 0.1%, or the asymptotic standard error of the fit parameters was larger than 0.01%, which was rarely the case for a sufficient numerical resolution.

### 3.6. *Numerical tests*

Each block of the algorithm was carefully tested in the course of the program development. The program passed the following two tests. First, we considered a test basic flow with angular velocity $\Omega = 10\cos(\pi z/2)\cos(\pi r/2)$ and the meridional stream function $\psi = -1.25(1+\cos(\pi z))(1+\cos(\pi r))zr^2$. A divergence-free test solution

$$\tilde{\boldsymbol{v}}(r,z)\,\mathrm{e}^{\mathrm{i}(m\phi+\sigma t)} \tag{3.13}$$

satisfying the no-slip condition as well as appropriate pole conditions was constructed in the form of a low-order polynomial (3.9)–(3.12) that was inserted in equation (2.1). After some algebra an expression for a formal periodic body force

$$\boldsymbol{f}(r,z)\,\mathrm{e}^{\mathrm{i}(m\phi+\sigma t)} = (\mathrm{i}\sigma\tilde{\boldsymbol{v}} + \tilde{\boldsymbol{\omega}} \times \tilde{\boldsymbol{U}} + \tilde{\boldsymbol{\Omega}} \times \tilde{\boldsymbol{v}} + \nabla \times \nabla \times \tilde{\boldsymbol{v}} + \nabla\tilde{P})\,\mathrm{e}^{\mathrm{i}(m\phi+\sigma t)}$$

was obtained that supports (3.13). This formal periodic body force is defined up to an arbitrary gradient of a scalar $\tilde{P}$. We chose this scalar so that $f_\phi = 0$. The values of $\sigma$ and $R$ were 20 and 1.5, respectively. The equations were integrated up to the time $t = 2$. The solution obtained was compared to the exact test solution (3.13) for different temporal and spatial ($N = M$) resolutions. We obtained an exponential or third-order convergence rate of the spatial or temporal approximation, respectively, as it can be observed in figure 1.

The second test considered the onset of the linear three-dimensional instability

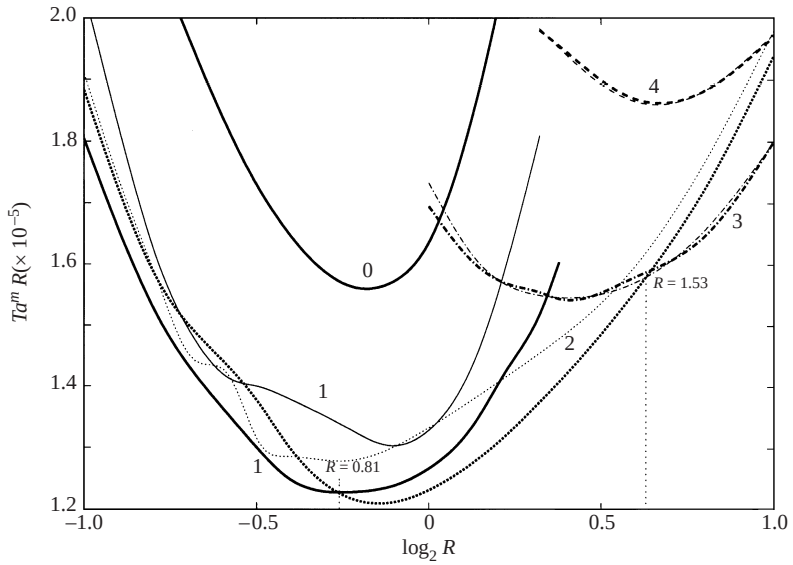


FIGURE 2. The neutral stability curves for various azimuthal modes. Thick and thin lines correspond to symmetric and antisymmetric perturbations, respectively. Note that for the purpose of a comprehensive presentation the product of Taylor number and aspect ratio is shown here.

of the rotating lid-driven flow in a cylinder with aspect ratio $R = 2/3.25 \approx 0.615$ as recently reported by Gelfgat *et al.* (2001). The model boundary conditions were defined by $\boldsymbol{U}(r,1) = \Omega_0 Rr(1-\exp(50(r^4-1)))\boldsymbol{e}_\phi$ at the top ($z = 1$) and zero elsewhere on $\mathscr{D}$. Since the basic solution no longer had vertical symmetry our algorithm was modified to full vertical coordinate $z$ expansions instead of the separation between equations (3.1)–(3.3) and equations (3.4)–(3.6). The basic flow was evaluated as the steady state of the time-dependent solution with a spatial resolution $55 \times 41$. We evaluated the leading eigenvalue for $m = 3$ for various spatial resolutions ($25 \times 13$, $29 \times 15$ or $33 \times 21$). The critical rotation rate $\Omega_0^{cr}$ was found as 7167, 7272 or 7275.6 with the oscillation frequency $-2118$, $-2147.8$ or $-2147.8$ for the different resolutions, respectively. The other modes with $m = 1, 2, 4$–6 had negative growth rates. Compared to Gelfgat *et al.* (2001) the critical lid rotation rate differed by 0.4%, which can be attributed to the smoothed specification of the boundary condition. The oscillation frequency of the critical perturbation agreed within 0.05% tolerance.

## 4. Results

Aspect ratios in the range $0.5 < R < 2$ were considered at the maximum spatial resolution $51 \times 41$. The neutral stability curves $Ta^m(R)$ were evaluated as roots of $\lambda_r(Ta, R, m)$ for $m = 1 - 4$ (figure 2). Higher modes with $m > 4$ had distinctly lower, and monotonically decreasing with $m$, negative growth rate $\lambda_r$ at the critical control parameter $Ta^{cr} = \min_m(Ta^m)$. Azimuthal wavenumbers up to $m = 15$ were considered for selected aspect ratios $R = 0.5, 1$ or 2. A few examples of the convergence of the critical parameters are given in table 1.

The instability onset was observed with the azimuthal wavenumber $m = 1$ and an approximately constant angular frequency $\lambda_i^{cr} \approx 650$ (figure 3) for elongated cylinders with $R \leqslant 0.81$. In this range of $R$ the $m = 2$ mode became unstable almost simultaneously with $\lambda_i^{cr} < 0$. The negative frequency means co-rotation of the

| $R = 0.5$, $m = 1$ | | | $R = 1.0$, $m = 2$ | | | $R = 2.0$, $m = 3$ | | |
|---|---|---|---|---|---|---|---|---|
| $N \times M$ | $Ta^{cr}$ ($\times 10^{-5}$) | $\lambda_i^{cr}$ | $N \times M$ | $Ta^{cr}$ ($\times 10^{-5}$) | $\lambda_i^{cr}$ | $N \times M$ | $Ta^{cr}$ ($\times 10^{-5}$) | $\lambda_i^{cr}$ |
| $37 \times 25$ | 3.598 | 693.2 | $33 \times 23$ | 1.238 | −162.8 | $31 \times 25$ | 0.892 | −249.0 |
| $41 \times 27$ | 3.618 | 694.3 | $39 \times 27$ | 1.231 | −160.40 | $35 \times 29$ | 0.9017 | −251.2 |
| $45 \times 29$ | 3.610 | 693.4 | $45 \times 33$ | 1.232 | −160.42 | $41 \times 35$ | 0.9019 | −251.62 |
| $51 \times 31$ | 3.612 | 693.6 | $51 \times 37$ | 1.232 | −160.42 | $51 \times 41$ | 0.9020 | −251.65 |

TABLE 1. Convergence of the critical parameters.

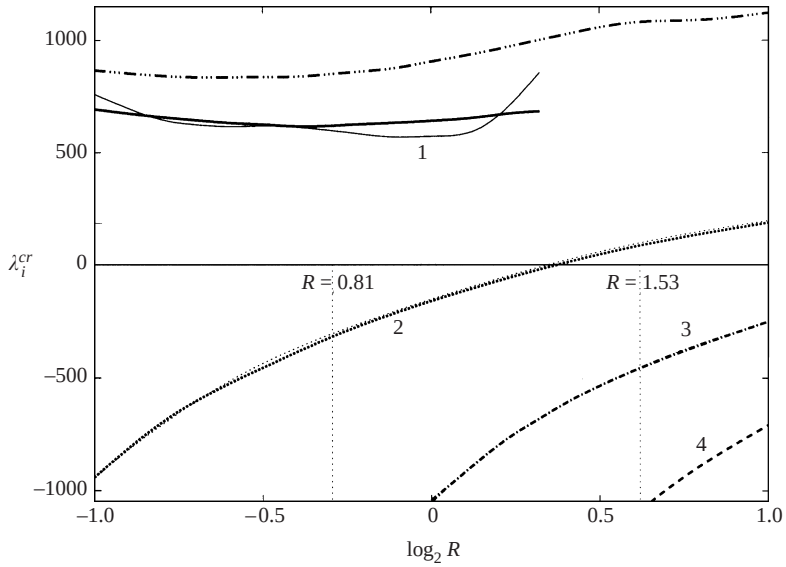


FIGURE 3. Frequency of neutrally stable modes vs. aspect ratio. —···—, The critical Reynolds number $Re = \max(U_\phi)H_0/\nu$.

perturbation with respect to the direction of the azimuthal flow. The absolute value of this frequency decreased for increasing $R$ and became distinctly lower in comparison to the frequency of the mean flow rotation in the range $0.81 < R < 1.53$ where the $m = 2$ mode was dominating. The $m = 3$ co-rotating mode prevailed for $R > 1.53$. The antisymmetric perturbation $v^-$ typically had a higher neutral stability limit than the corresponding $v^+$ for $m = 1, 2$, whereas the leading eigenvalues of the symmetric and antisymmetric perturbations were almost identical for $m = 3, 4$. The amplitude of the critical perturbation and its phase dynamics are shown in figure 4(*a–i*) for aspect ratios $R = 0.5, 1$ and 2.

## 5. Discussion

The three-dimensional instability always sets in prior to the linear axisymmetric instability for the aspect ratios considered. The azimuthal wavenumber of the critical perturbation increases with the relative diameter $R$. These two observations constitute an important difference to the lid-driven flow, where the most unstable perturbation is axisymmetric in the range $0.725 < R < 1.23$ and has a higher azimuthal wavenumber

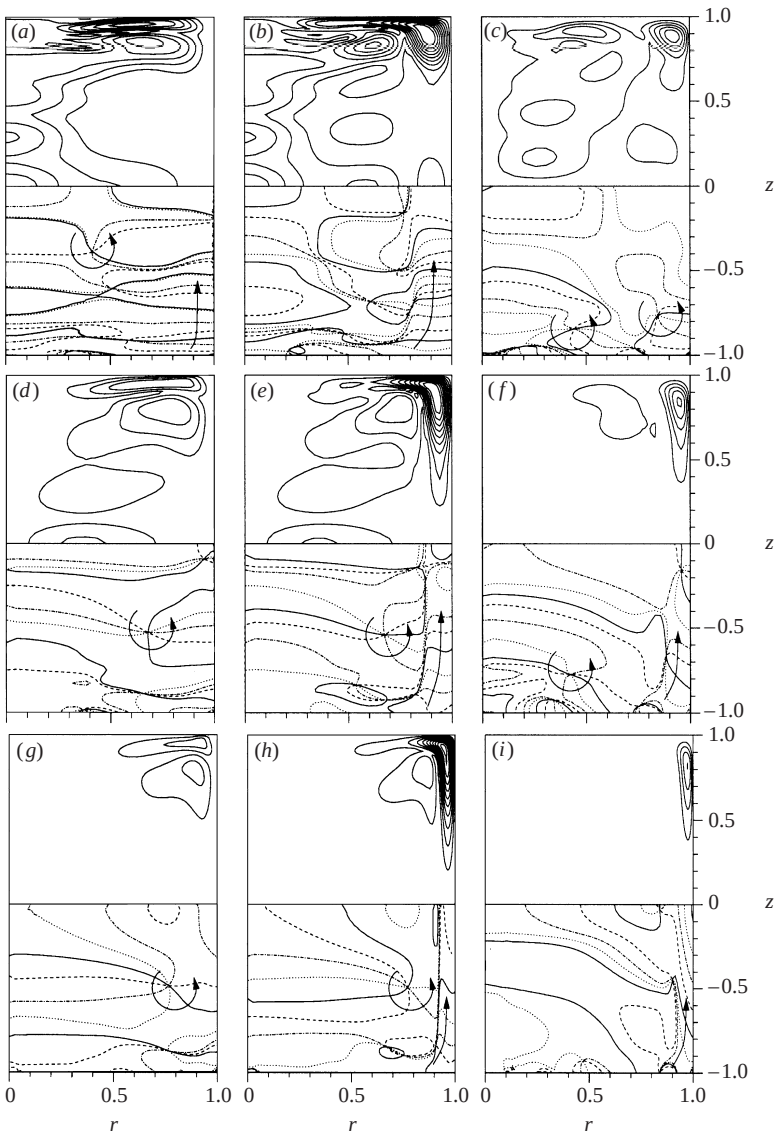


FIGURE 4. The critical perturbation normalized to $\max|v_\phi| = 1$: radial, azimuthal and axial velocity for $R = 0.5$, $m = 1$ ($a$–$c$); $R = 1$, $m = 2$ ($d$–$f$); $R = 2$, $m = 3$ ($g$–$i$). The upper part of each plot depicts the perturbation amplitude with isoline step 0.1. The lower part depicts the zero isoline of the perturbation for phase shift 0, $\pi/4$, $\pi/2$ and $3\pi/4$ with solid, dashed, dash-dotted and dotted lines, respectively.

($m = 4$ or 3) in an elongated cylinder. In the present RMF-driven flow the $m = 2$ mode shows a remarkably low frequency: $|\lambda_i^{cr}| \ll \Omega_0$. We found the change of the frequency sign at practically the same aspect ratio $R = 1.30$ as reported by Gelfgat *et al.* (2001) for the lid-driven flow. Thus, a bifurcating steady three-dimensional solution may be observed close to this aspect ratio in both cases. There is a variation of the velocity perturbation in the $z$-direction (similar to that in figure 4$d$–$f$ for $R = 1$) in the almost rigidly rotating core of the basic flow. It might be mistakenly regarded as a contradiction of the Taylor–Proudman theorem which states that an

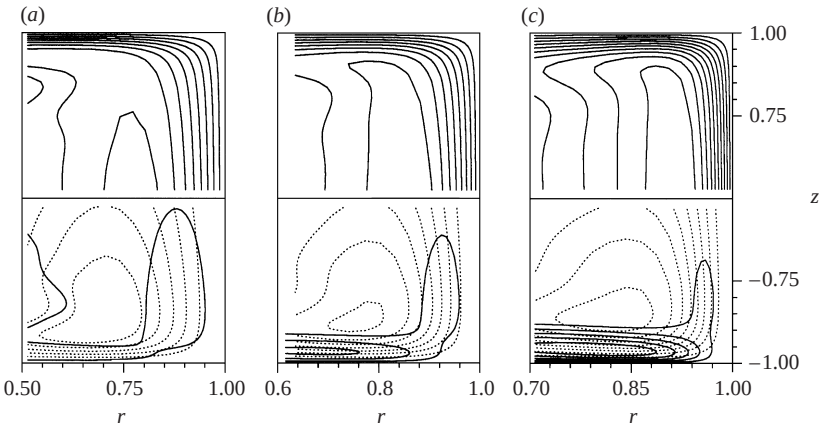


FIGURE 5. The basic flow at near-critical forcing in the corner for (*a*) $R = 0.5$, $Ta = 3.61 \times 10^5$; (*b*) $R = 1$, $Ta = 1.23 \times 10^5$; and (*c*) $R = 2$, $Ta = 0.903 \times 10^5$. The upper and lower part of each plot depicts the azimuthal velocity $U_\phi$ and the absolute velocity of meridional motion $(U_z^2 + U_r^2)^{1/2}$, respectively. The isoline step is 100. Dotted lines depict streamlines of the meridional flow.

almost rigidly rotating inviscid flow allows no quasi-steady perturbation varying along the axis of rotation. However, the theorem is stated in the rotating frame, where the three-dimensional perturbation is unsteady. Thus, the steady perturbation is, in fact, an inertial wave counter-rotating with respect to the inviscid core with exactly the same angular velocity. The experimental instability investigation of an RMF-driven liquid metal flow would be more complicated than the lid-driven flow where a transparent liquid might be used. In both cases, the measurement techniques should not perturb the flow. As a result one may have to deal with very low signals obscured by the instrument noise and possible axisymmetric nonlinear flow effects. However, the particularly low eigenfrequency of the $m = 2$ mode may serve as its signature under such circumstances since the axisymmetric modes have frequencies closer to $\Omega_0$.

There is a close similarity of the three-dimensional instability to its axisymmetric counterpart. Both can be discussed as follows. Since the instability has the largest amplitude in the corner, one may conclude that it originates there. Indeed, the thickness of the side layer increases towards the corner, making it more unstable. Besides, the secondary flow imposes an additional centrifugal force due to the rotation in the meridional plane. The trajectories of fluid particles are spirals wound on the irregular tori $\psi(r, z) = \text{const}$ (dotted lines in figure 5). Although the meridional flow may be considerably slower than the azimuthal rotation (especially for small $R$) the small radius of the streamline bending compensates this in the expression for the centrifugal force. Thus, the meridional basic flow adds a considerable contribution to the centrifugal forces being outweighed by the pressure gradient. Such a balance is known to be unstable if the circulation square decreases outwards (Rayleighs' criterion). The corner is just a small part of the whole volume where the strong meridional flow instantly washes away the perturbation. To grow as a whole, the perturbation may be a wave propagating upstream or it needs a certain feedback 'communication'. Both can be observed to a different extent by inspection of the perturbation phase dynamics (figure 4, arrows mark the phase velocity direction). The second option is provided by the inviscid core. From an infinite family of inertial waves the one is selected that properly resonates with the perturbation in both boundary

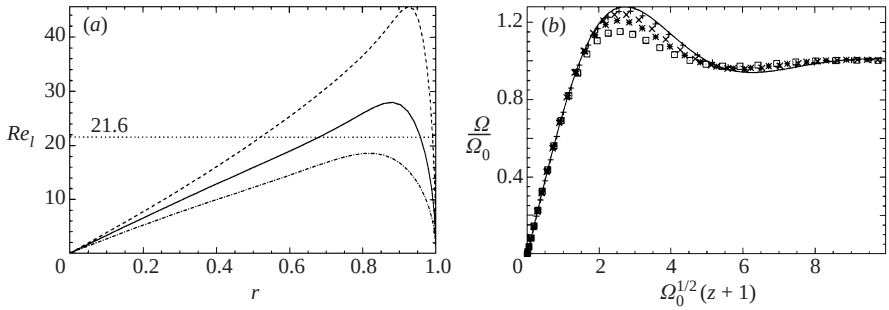


FIGURE 6. (*a*) The local Reynolds number vs. radius in the near-critical basic flow. The dashed, solid and dash-dotted curves correspond to $R = 2, 1$ and 0.5, respectively. (*b*) The angular velocity in the horizontal layer for $R = 2$. Symbols $+$, $\times$, $*$ $\boxdot$ correspond to $r = 0$, 0.5, 0.61 and 0.71, respectively. The solid line depicts the Bödewadt solution.

layers, thus supporting a certain feedback from the horizontal to the vertical layer over the core.

How far does the three-dimensional instability extend if the length of the cylinder increases? A quantitative answer to this question may be random due to the non-normal–nonlinear transition. We have shown (Grants & Gerbeth 2001) that the sensitivity of the flow to finite axisymmetric disturbances increases with the relative height of the cylinder. Therefore, we did not perform the linear stability analysis for an elongated cylinder $R < 0.5$ since the nonlinear transition is expected to prevail then. The question of whether the flow stays axisymmetric or also involves three-dimensional modes during the nonlinear transition is beyond the scope of this article.

Let us illustrate the results obtained in dimensional terms with an example of recently published (Volz & Mazuruk 2001) temperature measurements in RMF-driven liquid gallium flow heated from below. For a sufficiently strong forcing the onset was observed at $Ta = 1.5 \times 10^5$ independent of the imposed thermal gradient. With $\nu = 3.19 \times 10^{-7}\,\mathrm{m^2\,s^{-1}}$, $R_0 = H_0 = 1.2\,\mathrm{cm}$, the maximum azimuthal velocity of the near-critical flow is around $2.5\,\mathrm{cm\,s^{-1}}$. The signal from the thermistors was periodic and contained several frequencies: multiples of $f_0 = 0.12\,\mathrm{Hz}$. According to our analysis the frequency of the $m = 2$ and $m = 1$ modes is 0.055 Hz ($\lambda_i = -156$) and 0.26 Hz ($\lambda_i = 725$), respectively at $Ta = 1.5 \times 10^5$. The instability occurred below the axisymmetric limit and had a low frequency, in qualitative agreement with conclusions of the present analysis.

Instability of the Bödewadt layer was first observed experimentally in a spin-down flow by Savaş (1987) who reported the onset in the form of circular waves $m = 0$ at the local Reynolds number $Re_l = \Omega_0^{1/2} Rr = 25$. This agrees well with the absolute instability criterion $Re_l^{cr} = 21.6$ with a local azimuthal wavenumber $\beta^{cr} = -0.117$ obtained by Lingwood (1997) in a parallel flow approximation. Note, that the true azimuthal wavenumber $m = |[\beta^{cr} Re_l^{cr}]| = 2$ is too small to be correctly distinguished from 0 in this approximation. The small radial wavenumber $\alpha^{cr} = 0.34$ reported is in disagreement with the parallel flow approximation at such a low local Reynolds number. Indeed, the radial wavelength $2\pi/\alpha^{cr} = 18.5 \approx Re_l^{cr}$ is comparable to the critical radius. The non-parallel effects were included into the analysis by Fernandez-Feria (2000) who reported two instability modes, one with a considerably higher local radial wavenumber $\alpha \approx 0.6$ for large local Reynolds numbers and $\alpha^{cr} \approx 0.48$ at $Re_l^{cr} \approx 20$. We did not observe this instability in the near-critical RMF-driven flow,

although the local Reynolds number exceeded $Re_l^{cr}$ at two times and the boundary layers were well developed (figure 6). We see two reasons for this: (i) the influence of the finite aspect ratio suppresses the boundary layer instability, see the experimental results by Gauthier, Gondret & Rabaud (1999) or the numerical evidence by Lopez & Weidman (1996); (ii) the region with $Re_l > Re_l^{cr}$ and a developed Bödewadt layer is too narrow: only one wavelength (with $\alpha = 0.6$) fits into $0.5 < r < 0.8$ where both conditions are fulfilled (figures 5*c*, 6*a*).

## 6. Conclusions

The rotating-magnetic-field-driven flow in a cylinder becomes unstable first to non-axisymmetric, azimuthally periodic perturbations at diameter-to-height ratios $R$ between 0.5 and 2. The azimuthal wavenumber $m$ of the first instability increases with $R$ from 1 to 2 and from 2 to 3 at $R = 0.81$ and 1.54, respectively. Although the inherent Bödewadt layers seem thin and pronounced, the related boundary layer instability approaches do not apply since in the present RMF-driven case these layers are still too thick or not sufficiently developed in the near-critical flow. The instability originates in the cross-section of both rotating layers and involves a complicated interaction with inertial waves in the inviscid core. Hence, the instability is essentially global and its quantitative properties cannot be extrapolated to related flows as one can see by comparison to the lid-driven flow.

The authors appreciate productive discussions with V. Shatov concerning the numerical techniques.

## REFERENCES

Canuto, C., Hussaini, M. Y., Quarteroni, A. & Zang, T. A. 1988 *Spectral Methods in Fluid Dynamics*. Springer.

Escudier, M. P. 1984 Observations of the flow produced in a cylindrical container by a rotating endwall. *Exps. Fluids* **2**, 189–196.

Fernandez-Feria, R. 2000 Axisymmetric instabilities of Bödewadt flow. *Phys. Fluids* **12**, 1730–1739.

Gauthier, G., Gondret, P. & Rabaud, M. 1999 Axisymmetric propagating vortices in the flow between a stationary and a rotating disk enclosed by a cylinder. *J. Fluid Mech.* **386**, 105–126.

Gelfgat, A. Yu., Bar-Yoseph, P. Z. & Solan, A. 2001 Three-dimensional stability of axisymmetric flow in a rotating lid-cylinder enclosure. *J. Fluid Mech.* **438**, 363–378.

Goldhirsch, I., Orszag, S. A. & Maulik, B. K. 1987 An efficient method for computing leading eigenvalues and eigenvectors of large asymmetric matrices. *J. Sci. Comput.* **2**, 1, 33–58.

Grants, I. & Gerbeth, G. 2001 Stability of axially symmetric flow driven by a rotating magnetic field in a cylindrical cavity. *J. Fluid Mech.* **431**, 407–426.

Grossmann, S. 2000 The onset of shear flow turbulence. *Rev. Mod. Phys.* **72**, 603–618.

Lingwood, R. J. 1997 Absolute instability of the Ekman layer and related rotating flows. *J. Fluid Mech.* **331**, 405–428.

Lopez, J. M. & Weidman, P. D. 1996 Stability of stationary endwall boundary layers during spin-down. *J. Fluid Mech.* **326**, 373–398.

Saric, W. S. 1994 Görtler vortices. *Annu. Rev. Fluid Mech.* **26**, 379–409.

Savaş, Ö. 1987 Stability of Bödewadt flow. *J. Fluid Mech.* **183**, 77–94.

Tomasino, Th. & Marty, Ph. 2000 Numerical simulation of 3D flows induced by a rotating magnetic field. In *Proc. Fourth Intl Conf. on Magnetohydrodynamic* (ed. A. Alemany), vol. 1, pp. 245–249.

Tuckerman, L. S. 1989 Divergence-free velocity fields in nonperiodic geometries. *J. Comput. Phys.* **80**, 403–441.

Volz, M. P. & Mazuruk, K. 2001 An experimental study of the influence of a rotating magnetic field on Rayleigh–Bénard convection. *J. Fluid Mech.* **444**, 79–98.